International Journal of Plasticity 97 (2017) 126–144

Contents lists available at ScienceDirect

International Journal of Plasticity

journal homepage: www.elsevier.com/locate/ijplas

Dislocation core effects on slip response of NiTi- a key to understanding shape memory

S. Alkan, H. Sehitoglu*

Department of Mechanical Science and Engineering University of Illinois, Urbana, IL 61801, United States

ARTICLE INFO

Article history:
Received 12 April 2017
Received in revised form 25 May 2017
Accepted 27 May 2017
Available online 31 May 2017

ABSTRACT

The understanding of the non-Schmid behavior in shape memory alloy NiTi is considered a significant breakthrough because this alloy still remains enigmatic. We utilize an Eshelby-Stroh formalism in conjunction with Molecular Statics-Peierls stress calculation to predict the experimental CRSS results for three different crystal orientations and tension-compression cases. These combination of tools incorporating elastic anisotropy and core displacements are necessary to develop a precise understanding of non-Schmid behavior. We note the different extents of core spreading produce a highly asymmetric tension-compression behavior and strong orientation dependence governed by the non-glide shear and normal stress components. The experimental results and empiricism free modeling produces excellent agreement, and most importantly enlisting scientific insight into the shape memory response.

1. Introduction

It is well known that the slip behavior of SMAs plays a key role in transformation response as it affects internal stress evolution (Chowdhury and Sehitoglu, 2017b), the transformation strains (Sehitoglu et al., 2003) and transformation hysteresis (Hamilton et al., 2004). Previous work has identified the complexity of the slip behavior including the orientation (Surikova and Chumlyakov, 2000) and tension-compression effects (Sehitoglu et al., 2000), yet a model for CRSS (Critical Resolved Shear Stress) has not emerged. The problem deserves considerable attention as understanding the shape memory alloys remains an anathema to researchers in mechanics and materials science. To appreciate the complexity of slip response in SMAs, we must first revisit the body centered cubic (bcc) metals -alloys and discuss the deviations from Schmid Law (Duesbery and Vitek, 1998; Gröger et al., 2008b; Vitek, 1974). We review below bcc alloys and then focus on the modeling of shape memory alloy, NiTi.

The slip initiation in the classical plasticity theory is developed based on two assertions, commonly denoted as Schmid Law (Schmid and Boas, 1950; Taylor, 1934), i.e. (i) the activation of the slip system on the closest packed plane along the densest atomic packing direction and (ii) the initiation of slip is determined by the critical value of resolved shear stress along Burgers' vector, i.e. CRSS. These assertions have been successful in explaining the slip initiation along <110> {111} family system in face centered cubic (fcc) and the basal system <1120> {0001} in hexagonal packed crystal (hcp) structure pure metals (Christian, 1983; Duesbery, 1989). On the other hand, the complex plastic response of the bcc metallic materials has been a quandary for the researchers since the early experimental work of Taylor on iron and β brass (Taylor, 1928) exhibiting

* Corresponding author.
E-mail address: huseyin@illinois.edu (H. Sehitoglu).

http://dx.doi.org/10.1016/j.ijplas.2017.05.012
0749-6419/

significant deviations from the Schmid Law. The unavailability of crystallographic parameters to characterize the structure of the defects accommodating the plastic strain, i.e. dislocations, was the major obstacle at that time.

The advancements in the atomistic simulation of materials in the last few decades opened new frontiers in developing a better understanding of slip deformation. This is especially true in unraveling the complex mechanical response of bcc materials. The topic has peaked the curiosity of a select of group of researchers Suzuki, Duesbery and Vitek (Duesbery, 1984; Duesbery et al., 1973; Suzuki, 1968; Vitek, 1974) who were among the first researchers to use computational tools to study the response of bcc metals. Today, the non-planar core structure of screw dislocations and the asymmetric Generalized Stacking Fault Energy-GSFE- profiles along the active glide systems are accepted to be responsible for the deviations from Schmid Law (Duesbery and Vitek, 1998). The works on ordered bcc alloys have also shown considerable deviations from the Schmid law, especially at low temperatures (Yamaguchi et al., 1981; Yamaguchi and Umakoshi, 1983). More recently, the work on ordered bcc alloys and specifically the shape memory alloys have been of significant interest (Alkan and Sehitoglu, 2017a,b). The ordered bcc in austenite phase (B2, DO_3 and $L2_1$ type) exhibits directional properties, i.e. orientation dependence of CRSS and tension-compression slip asymmetry, resulting in large deviations from the Schmid Law. Despite the importance of the topic of slip in SMAs, there has been a lack of research efforts on the role of core effects.

This work aims at unraveling the complex behavior of shape memory alloys where the transformation characteristics are significantly modified due to the underlying dislocation mediated slip (Chowdhury and Sehitoglu, 2016). The slip resistance depends on the core spreading and it is a function of stress state and crystal orientation (Gröger et al., 2008a) which is manifested by the interplay among the fractional dislocations (Vítek and Kroupa, 1969) composing the core structure. Because NiTi is one of the most significant shape memory alloys, we elucidated on its plastic behavior by incorporating both experimental measurements and theoretical analyses. Our present results and the studies reported in the literature (Benafan et al., 2013; Ezaz et al., 2013; Sehitoglu et al., 2017a,b; Simon et al., 2010) clearly identify that {110} <001> family system is predominantly active in the NiTi alloy. The detailed experimental measurements suggest the presence of non-Schmid behavior in B2 ordered NiTi (Alkan and Sehitoglu, 2017b) and stands out as a further motivation to interrogate the underlying mechanisms on theoretical grounds.

The paper is organized as follows: we introduce the Molecular Statics (MS) calculations within framework of Eshelby-Stroh (Eshelby et al., 1953; Stroh, 1958) formalism and evaluate the core structure in stress-free configuration and under the stress states corresponding to the <111>, <349>, <5 8 18>, <249>, <259>, <148>, <188>, <011> oriented samples (see Section 3). We have experimental data on 3 orientations under uniaxial tension-compression (6 cases) loading, i.e. <111>, <249> and <011> (Alkan and Sehitoglu, 2017b). Within a concerted fashion, we also generated the GSFE curves along the active {110} <001> glide system family to extract complimentary information about the slip energetics. Moreover, we developed a theoretical Peierls-Nabarro framework (Alkan and Sehitoglu, 2017a; Nabarro, 1947b; Peierls, 1940; Wang et al., 2014) to predict the CRSS values under uniaxial tension and compression along the corresponding crystallographic directions. We predict the significant tension-compression asymmetry of the slip and the orientation (including non-glide shear and normal stresses) dependence. There are no fitting parameters or adjustments in the modified Peierls-Nabarro model to fit the experimental data. Therefore, the work is aimed to construct a theoretical bridge between the experimental evidence collected for the plastic deformation characteristics of B2 NiTi and the underlying atomistic scale dislocation core mechanics, such that the multiscale physical phenomena entailing the non-Schmid effects observed in NiTi shape memory alloy can be studied in depth. As a last step, a modified yield criterion has been constructed based on the experimental and theoretical CRSS results.

2. Methods

2.1. Description of interatomic forces

In this study, the interatomic forces for generating the GSFE curve, also denoted as γ curve, and the modeling of the screw dislocation core structure are based on the many-body NiTi potential (Chowdhury et al., 2016; Ren and Sehitoglu, 2016) developed within the framework of generalized Finnis-Sinclair approach (Finnis and Sinclair, 1984; Mendelev et al., 2007). The details of the potential are elaborated in Appendix A with comparison of the lattice constant, a, equilibrium volume per atom per unit cell, V_0, and the independent elastic stiffness tensor components C_{11}, C_{12}, C_{44} (the fourth order C_{ijkl} stiffness tensor with $i, j, k, l = 1, 2, 3$ is shown in Voigt notation) of B2 NiTi predicted by the potential and the experimental measurements (Mercier et al., 1980; Sittner et al., 2003). As can be seen in Table A.1 and A.2, the predicted values exhibit close agreement with the experimental measurements in which the maximum difference is calculated to be in the elastic constant C_{11} by a relative difference of 9.8%. Considering the capability of the potential in predicting the linear elastic response and the crystallography of B2 NiTi, we utilized it to evaluate the slip energetics and the screw dislocation core shape in stress-free configuration and under different stress states.

2.2. Generation of GSFE curves by molecular statics (MS)

In order to develop a comprehensive understanding of the slip characteristics along the experimentally observed active {110} <001> family system in B2 NiTi, we generated the GSFE curves within framework of MS at 0 K. To accomplish this task,

we delineated a simulation box of 90 × 90 × 90 Å^3 size with periodic boundary conditions along all three directions using LAMMPS (Large Scale Atomic/Molecular Massively Parallel Simulator) software (Plimpton, 1995) and incrementally sheared the top and bottom half-crystallite, i.e. denoted as Crystal A and Crystal B respectively, by an amount of equal and opposite displacements referred as u_A and u_B as in Fig. 1 (a) for the glide system [001] (110). The applied disregistry, defined as $u = u_A - u_B$ is implemented incrementally within range of 0 to a [001] and the atoms are allowed to relax along all but the shearing direction under the interatomic force field defined by the potential utilized. This is a new potential introduced recently (Ren and Sehitoglu, 2016) which will be discussed also in Appendix A.

Fig. 1 (b) shows the GSFE curve which has only a single maximum suggesting an unstable stacking fault energy value of $\gamma^{us} = 200.5$ mJ/m^2 at a disregistry level of a/2<001>. The absence of a local minimum implies that no stable stacking faults are allowed in B2 NiTi on <001> {110} family systems. This result also complies with the first-principles calculations reported in an earlier of study of Ezaz et al. (2013).

2.3. Screw dislocation core calculations by molecular statics

Following the experimental results of our previous published work on plasticity of B2 NiTi at 293 K addressing the glide motion of dislocations along <001> {110} family slip systems (Sehitoglu et al., 2017a,b), we focused on the core structure of a<001> screw dislocations in stress-free configuration and under applied stress field. To that end, we delineated a simulation box of 150 × 150 × 3 Å^3 and introduced a screw dislocation with Burgers' vector **b** = a [001] at the geometric center utilizing the Eshelby-Stroh formulation as illustrated in Fig. 2 at four steps (a, b, c and d).

As an initial step, as shown in Fig. 2(a), the screw dislocation is introduced within the framework of anisotropic linear elasticity by the following displacement formulation in Eq. (1) (with k, n = 1,2,3) where x_1 and x_2 are the initial coordinates of the lattice points given with respect to the $x_1 - x_2 - x_3$ frame shown in Figs. 3 and 4 (Eshelby et al., 1953; Stroh, 1958).

$$u_k^o(x_1, x_2) = \mathrm{Re}\left[\frac{-1}{2\pi\sqrt{-1}}\sum_{n=1}^{3} A_k^n D^n \log(x_1 + p_n x_2)\right] \tag{1}$$

In Eq. (1), the three p_n coefficients are the roots of the expression of Eq. (2) and they are chosen among the three complex-conjugate pairs satisfying:

$$\det\left(L_{i1m1} + L_{i1m2}p_n + L_{i2m1}p_n + L_{i2m2}p_n^2\right) = 0 \tag{2}$$

where L_{ijkl} is calculated by transforming the fourth order elastic stiffness tensor, i.e. $L_{ijkl} = Q_{im}Q_{jn}Q_{kp}Q_{lr}C_{mnpr}$, with summation convention implied, into the dislocation frame$x_1 - x_2 - x_3$. On the other hand, for each p_n value, there corresponds a vector of A_k^n satisfying Eq. (3).

$$\left(L_{i1k1} + L_{i1k2}p_n + L_{i2k1}p_n + L_{i2k2}p_n^2\right)A_k^n = 0 \tag{3}$$

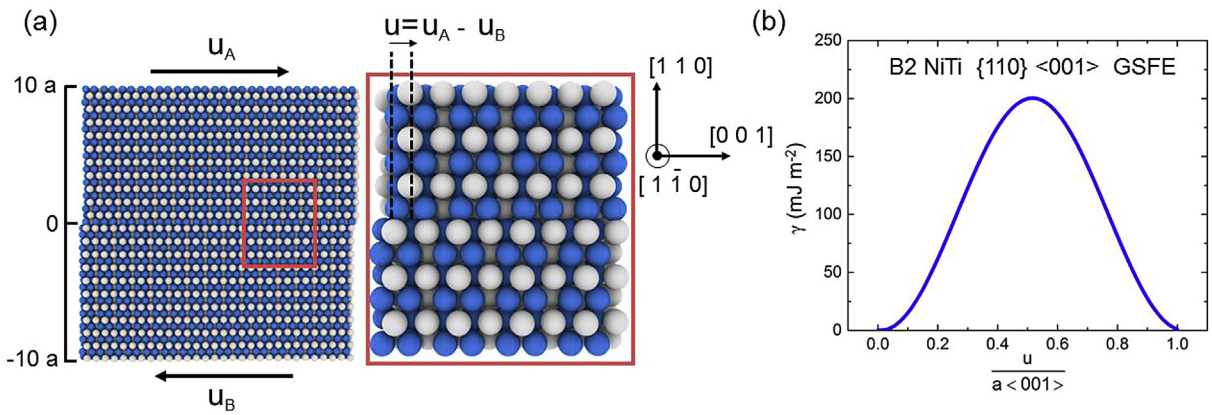

Fig. 1. The GSFE (γ) curve is generated by MS for an equi-atomic composition B2 ordered NiTi by shearing along the two semi-infinite crystals along the glide system [001] (110). In **(a)**, the (110) glide plane is located at 0 position along the vertical axis parallel to [110] direction and separates the two semi-infinite crystallite which are denoted as Crystal A (above the (110) glide plane) and Crystal B (below the (110) glide plane). Both A and B crystals are sheared by the homogeneous, equal and opposite direction of displacements, i.e. u_A and u_B. The relative shear displacement of the Crystal A with respect to Crystal B is denoted byu, i.e. equal to $u_A - u_B$. Ovito software is utilized for the visualization (Alexander, 2010). **(b)** The resulting GSFE curve for equi-atomic B2 NiTi under varying disregistry u between 0 and |a[001]| is plotted. The atoms are allowed to relax only along [110] and [1$\bar{1}$0] directions.

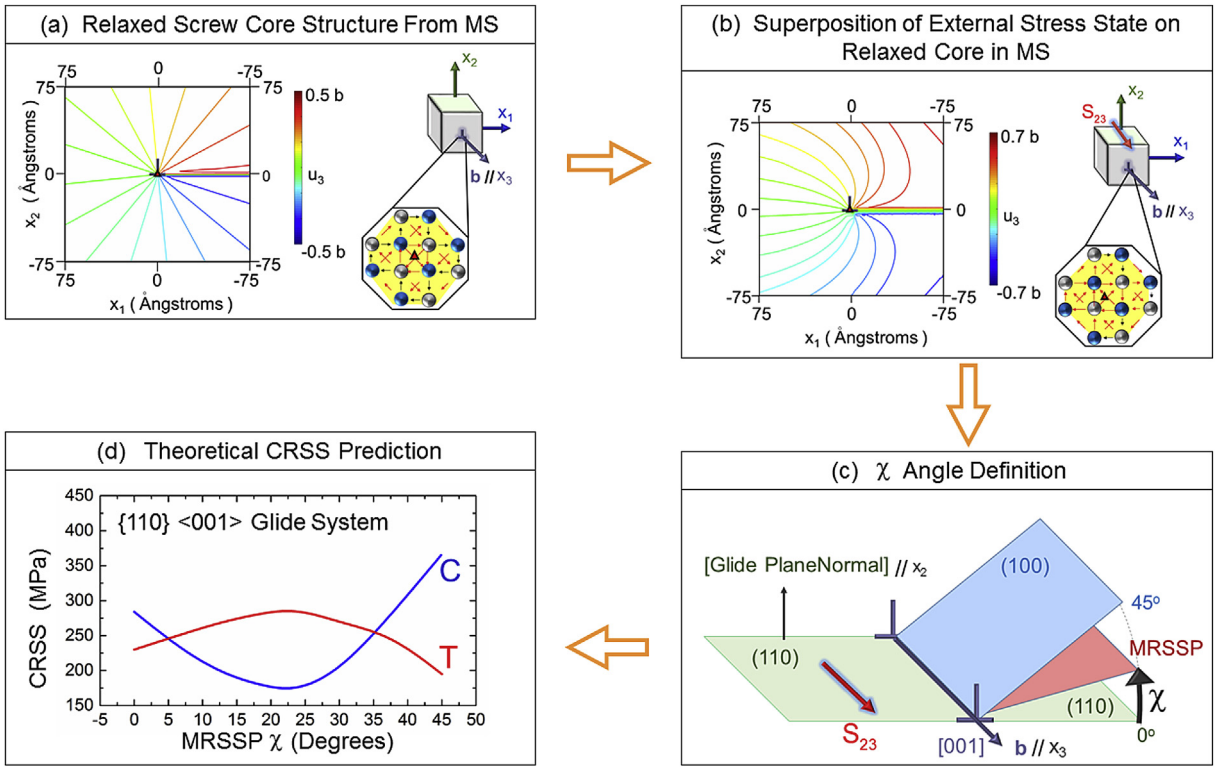

Fig. 2. The methodology followed to calculate the screw dislocation core shape in stress-free and under a homogeneous external stress state is summarized. (a) As a first step, a screw dislocation with a prescribed Burgers' vector, **b**, is introduced inside the simulation box using the sextic displacement field formulation of Eshelby-Stroh. Following this step, to calculate the core shape in stress-free configuration, the simulation box is relaxed. The core displacements that are shown as inset will be explained later. (b) In order to interrogate the dislocation core structure under a homogeneous external stress field, the corresponding displacement field defined within the framework of anisotropic elasticity is superposed incrementally on the stress-free configuration shown in (a). (c) The MRSSP plane, Burgers vector, glide shear stress, the characteristic angle χ are depicted. (d) The externally stressed structure is relaxed after each increment and this iterative procedure is repeated until the dislocation center translates by an integer multiple of lattice spacing. The theoretical CRSS value is evaluated based on a modified Peierls-Nabarro model developed and it is plotted using the χ angle convention. The theoretical CRSS values exhibit both crystal orientation dependency and tension-compression asymmetry.

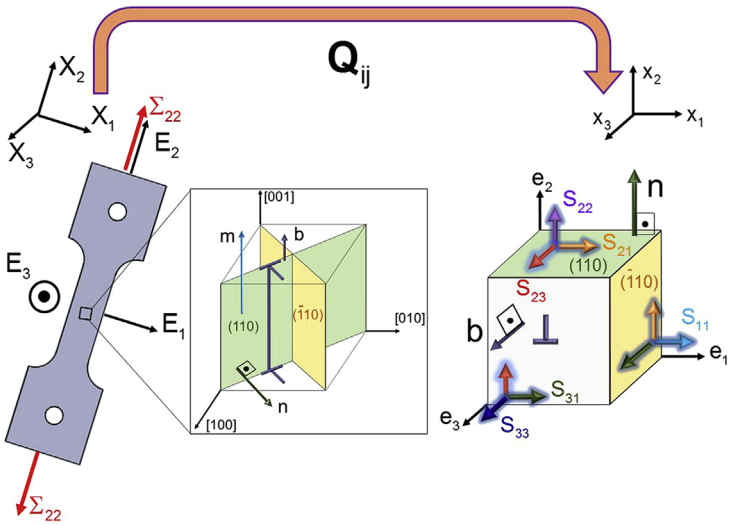

Fig. 3. Illustrates the specimen coordinate frame $X_1 - X_2 - X_3$, the cubic crystal coordinate frame [100]-[010]-[001] and the local dislocation coordinate frame $x_1 - x_2 - x_3$ for a tension sample under action of Σ_{22}. **n** and **m** vectors are the unit glide plane normal and the unit slip direction vectors respectively. The transformation of coordinates from $X_1 - X_2 - X_3$ to $x_1 - x_2 - x_3$ frame is accomplished by the transformation matrix **Q**. Moreover, the components of the deviatoric stress tensor **S** are also shown in $x_1 - x_2 - x_3$ frame.

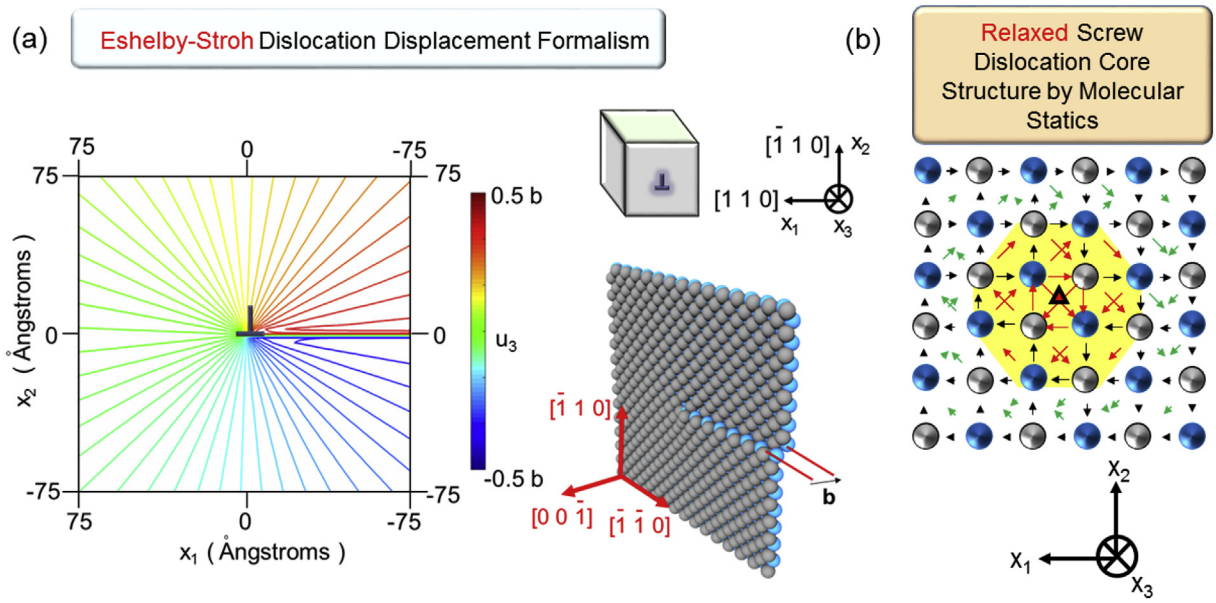

Fig. 4. Shows the displacement field parallel to the Burgers' vector **b** from the Eshelby-Stroh formalism in the stress free configuration of a screw dislocation with **b** = a [001]. The relaxed core displacements parallel to **b** obtained from MS simulation with the initial displacement field provided in (a) is shown by utilizing DDMT. Each arrow represents the relative displacement vector between the connected atoms. The magnitude of the arrows are in proportion with the relative displacement vector norm such that the arrows are normalized with |a/2[001]| magnitude. For the diagonal neighboring atoms green arrows are utilized. For relative displacements greater than |a/6[001]|, the atoms are colored in red with a yellow background. As can be seen, the stress-free screw dislocation core is extended over three ($\bar{1}10$) plane. (For interpretation of the references to colour in this figure legend, the reader is referred to the web version of this article.)

As Eq. (2) holds, not all three of the components vector A_k^n (corresponding to each p_n) can be solved uniquely. Therefore following the convention in (Lothe, 1992), one of the A_k^n component is set equal to 1 for each n (preferably A_3^n if $A_3^n \neq 0$). Moreover, three D^n complex constants expressed in the boundary conditions of Eqs. (4)–(5) are also necessary to be solved (Re [ ]: real part of the expression inside the square brackets).

$$\mathrm{Re}\left[\sum_{n=1}^{3} A_k^n D^n\right] = b_k \tag{4}$$

$$\mathrm{Re}\left[\sum_{n=1}^{3}\left(L_{ijk1} + L_{ijk2}p_n\right)A_k^n D^n\right] = 0 \tag{5}$$

Physically, the expression in Eq. (3), provides the set of equations satisfying the equilibrium conditions as well as small strain-displacement relationship within the framework of anisotropic elasticity. On the other hand; as u_k^o is a multi-valued function, there is a jump by **b** vector in its value if any piecewise-smooth curve C enclosing the dislocation crosses the glide plane (i.e. described along $x_2 = 0$) for $x_1 < 0$ because of the slip step. Eq. (4) expresses this mathematical condition in algebraic form ensuring the condition of zero resultant force per unit length acting on curve C in Eq. (5) satisfied.

The stress field corresponding to u_k^o satisfies the equilibrium conditions within the framework of anisotropic linear elasticity. However, as the displacements inside the core region generally exceed the linear elastic limit, the equilibrium of interatomic forces can not be taken for granted. Therefore, the equilibrium of interatomic forces is incorporated by implementing a relaxation procedure within the framework of the interatomic potential. In the force equilibrating scheme, the atoms located on the outer planar boundaries of $\pm(1\bar{1}0)$ and $\pm$ (110) are fixed in their displaced positions. The rest of the atoms are relaxed with the periodic boundaries conditions on the outer surfaces of $\pm$ (001).

The relaxation procedure equilibrates the interatomic forces and results in significant deviations from the linear elastic solution introduced in Eq. (1) especially within the proximity of the dislocation core. The details of the relaxed core structure calculated by MS is emphasized utilizing the displacement differentials between the neighboring atoms which is denoted as Differential Displacement Map Technique (DDMT) (Vítek et al., 1970). This representation forms the basis for visualization of core spreading. In this technique, the relative displacement vectors between the neighboring atoms parallel to **b** (which is equal to u_3 in this study as $\mathbf{b}//\mathbf{e_3}$) are shown with the projected arrows connecting these two corresponding atoms on the plane normal to **b**. Of note is that the magnitude of the arrows is normalized to a maximum value of $|a/2<001>|$. As can be seen in the octagon-shaped inset of Fig. 2 (a), the displacements are concentrated on multiple ($\bar{1}10$) planes suggesting the

non-planar shape of the a [001] screw dislocation core in the **externally** stress-free configuration of B2 NiTi crystal. It should also be emphasized that even though the system is in externally stress-free configuration, an internal stress field owing to the presence of the screw dislocation exists.

As a next step, following the flow chart in Fig. 2 (b), a homogeneous external stress field is implemented on the system by incrementally superposing the corresponding displacement field defined within the framework of anisotropic elasticity upon the externally stress-free dislocation configuration. An important point to note at this stage is that although the Burgers' vector direction for a screw dislocation of |a <001>| strength residing on a {110} family plane in stress-free configuration possesses directionality invariant to the two fold symmetry; under an external stress state, the glide sense is of significant importance because of a potential interplay between the glide force acting on the dislocation and the stress tensor components (Duesbery, 1984; Peach and Koehler, 1950). For example, it is known that the core shape changes under different directional relations between the applied glide shear and non-glide shear stress components acting on the active glide plane in DO_3 ordered Fe_3Al (Alkan and Sehitoglu, 2017a). Therefore, for each sample orientation we focused, we changed the sense of **b** vector in the Eshelby-Stroh formulation to take the glide sense change under tension and compression loading into consideration. The orthonormal base vectors of $x_1 - x_2 - x_3$ frame, $\mathbf{e_1} - \mathbf{e_2} - \mathbf{e_3}$, as illustrated in Fig. 3, are related to the active glide system in each sample simulated such that $\mathbf{e_2}$ and $\mathbf{e_3}$ coincide with the glide plane normal, **n**, and the glide direction, **m**, vectors respectively. The base vector $\mathbf{e_1}$ can be determined by the vector cross-product of other two base vectors following right-hand rule. Below, Table 1 tabulates the active glide systems for each sample orientation along with the crystallographic directions of $\mathbf{e_1} - \mathbf{e_2} - \mathbf{e_3}$.

The applied stress tensor, $\mathbf{\Sigma}$ defined in the sample coordinate frame $X_1 - X_2 - X_3$, is of either uniaxial tension or compression state. The crystallographic directions of the orthonormal vector triad $\mathbf{E_1} - \mathbf{E_2} - \mathbf{E_3}$ which compose the set of base vectors in $X_1 - X_2 - X_3$ frame are tabulated in Table 1 and illustrated in Fig. 3 as well as Σ_{22} which is the only non-zero component of $\mathbf{\Sigma}$ tensor. Throughout this study, as hydrostatic pressure is evaluated to be of negligible effect, we will present the results of the atomistic scale calculations by using the deviatoric stress tensor, **S**, as illustrated in Fig. 3. The components of **S** are evaluated by transforming the deviatoric part of $\mathbf{\Sigma}$, i.e.$\mathrm{dev}(\mathbf{\Sigma}) = \mathbf{\Sigma} - 1/3\mathrm{trace}(\mathbf{\Sigma})\mathbf{I}$, from $X_1 - X_2 - X_3$ to $x_1 - x_2 - x_3$ frame (**I** is the second order identity tensor). In this transformation scheme, the coordinate transformation matrix components are given by $\mathbf{Q}_{ij} = \mathbf{e}_i \bullet \mathbf{E}_j$. Moreover, it should be noted that CRSS is directly equal to S_{23} component owing to the convention we introduced earlier. Throughout this work, we refer to S_{23} as glide stress (GS), S_{21} as non-glide shear stress (NGS), S_{11}, S_{22} and S_{33} as normal stresses (NS) and S_{13} as the conjugate plane stress.

The elastic displacement field resulting from the applied S tensor, u_k^e, can be expressed as in Eq. (6) where M_{kijm} represents the fourth order elastic compliance tensor defined as the inverse of the elastic stiffness tensor, C_{klmj}^{-1}.

$$u_k^e = \int_{-75}^{+75} M_{kijm} S_{jm} dx_i \qquad j, k, m = 1, 2, 3 \;\&\; i = 1, 2 \tag{6}$$

In the expression of Eq. (6), the bounds of the integration is dependent on the sample size in which case they are equal to +75 and -75 for the simulation box with an equal width and length of 150 Å utilized in this study. Upon superposition of the displacement field u_k^e on each atom inside the simulation box, the atoms on the planar boundaries of $\pm(1\bar{1}0)$ and $\pm(110)$ are fixed in their displaced positions meanwhile the rest of the atoms are relaxed with a max. force tolerance of 0.015 eV/Angstrom. The periodic boundary conditions on $\pm(001)$ planar boundaries are conserved. To initiate the glide motion of the screw dislocation and evaluate the corresponding CRSS values as shown in Fig. 2(d), the applied loading intensity is increased

Table 1
Tabulates the crystallographic orientations parallel to the orthonormal triads of $\mathbf{E_1} - \mathbf{E_2} - \mathbf{E_3}$ and $\mathbf{e_1} - \mathbf{e_2} - \mathbf{e_3}$ for each sample under uniaxial tension and compression.

Sample	$\mathbf{e}_1 - \mathbf{e}_2 - \mathbf{e}_3$	$\mathbf{e_1} - \mathbf{e_2} - \mathbf{e_3}$
<111> T	[1-2-1]-[-1 -11]-[-10-1]	[0-1-1] -[0-11]- [-100]
<111> C	[1-2-1]-[-1 -11]-[-10-1]	[011] -[0-11]- [100]
<349> T	[-16-3]-[349]-[33 9 7]	[110]-[-110]-[001]
<349> C	[-16-3]-[349]-[33 9 7]	[-1-10]-[-110]-[00-1]
<5 8 18> T	[-2 10 -5]-[-5 8 18]-[140 11 34]	[110]-[-110]-[001]
<5 8 18> C	[-2 10 -5]-[-5 8 18]-[140 11 34]	[-1-10]-[-110]-[00-1]
<249> T	[6167 -70]-[-924]-[8 6 15]	[110]-[-110]-[001]
<249> C	[6167 -70]-[-924]-[8 6 15]	[-1-10]-[-110]-[00-1]
<259> T	[2-11]-[-259]-[-7 -10 4]	[110]-[-110]-[001]
<259> C	[2-11]-[-259]-[-7 -10 4]	[-1-10]-[-110]-[00-1]
<148> T	[0-21]-[-148]-[-20 -1 -2]	[110]-[-110]-[001]
<148> C	[0-21]-[-148]-[-20 -1 -2]	[-1-10]-[-110]-[00-1]
<188> T	[01-1]-[-188]-[16 1 1]	[110]-[-110]-[001]
<188> C	[01-1]-[-188]-[16 1 1]	[-1-10]-[-110]-[00-1]
<011> T	[212]-[-101]-[1-41]	[0-11]-[011]-[-100]
<011> C	[212]-[-101]-[1-41]	[01-1]-[011]-[100]

incrementally. The core structure of the screw dislocation is captured with the corresponding relaxed atomic displacement field, u_k, intermittently up until just before the instant that the dislocation center translates by a distance of an integer multiple of lattice spacing. The corresponding core configurations will be analyzed thoroughly in the following sections.

In this study, the CRSS level is measured and calculated on the glide plane which belongs to {110} family. The CRSS values calculated at the instant of glide are plotted in Fig. 2 (d) by following the characteristic χ angle convention as illustrated in Fig. 2 (c) (Schulson and Teghtsoonian, 1969). Geometrically, χ angle is measured from the {110} family plane bearing the highest glide shear stress parallel to **b**, S_{23}, to the maximum resolved shear stress plane (MRSSP) which is the plane bearing the globally maximum S_{23} without any crystallographic restriction. Owing to the symmetry of B2 lattice structure along with the active {110} <001> glide system, the angle χ is bounded between 0° and 45° unlike the familiar -30° to 30° range for the bcc metals with the active glide system family of {110} <111>. At this stage, it is important to emphasize that there is another commonly used convention in the literature (Gröger et al., 2008a) which defines the CRSS value based on the shear stress acting parallel to the glide direction on MRSSP. However, we prefer to quantify the CRSS level on the glide plane as the physical dislocation glide incurs on the glide plane. The characteristic χ angle establishes the relation between the crystallographic direction along which the uniaxial loading is applied and the active glide system such that the orientation effect of the single crystal sample on the dislocation glide motion can be distinguished.

The screw dislocations that we focused in the 8 distinct crystallographic orientations under uniaxial tension and compression are subjected to different deviatoric stress states in the local dislocation frame $x_1 - x_2 - x_3$. As can be seen in Fig. 2(d), depending on the orientation, the CRSS level under compression is greater than tension or vice a versa. This non-Schmid trend in CRSS values are also substantiated by the uniaxial tension and compression experiments conducted on 3 sample orientations, i.e. <111>, <249> and <011>. The experimental measurements indicate that for the <111> and <011> orientated samples, the CRSS levels are greater under compression compared to tension. On the other hand, an opposite trend is observed for the <249> oriented samples. The experimental measurements of CRSS levels pertaining to these 3 samples unequivocally indicate that there is a significant differential in tension and compression which extends up to an experimental value of 120 MPa (>50% difference in stress) for the <011> oriented sample. This differential is lower for the <111> oriented sample which is 42 MPa. The <249> sample is located in between these two cases, by a differential of 85 MPa. Based on this experimental evidence addressing the anisotropy of the CRSS values along the same slip system family, i.e.{110} <001>, the dislocation core effects are surmised to prevail on the plastic slip behavior of B2 NiTi. Considering these opposite trends in CRSS values, we focused on the screw dislocation core structures posited in the <111> and <249> oriented samples via atomistic scale calculations. The results indicate that the CRSS levels to activate glide are affected by the applied stress state components owing to their interaction with the dislocation core displacements.

The deviation of CRSS values from the Schmid Law in B2 NiTi owing to the dislocation core shape change can be ascribed to two primary reasons manifested on both experimental and theoretical grounds. Firstly, the glide resistance is dependent on the single crystal orientation, even if only uniaxial compression or tension is considered. Secondly, there is a differential in the CRSS values corresponding to the identical crystallographic sample orientation under uniaxial compression and tension, namely tension-compression asymmetry. The detailed examination of these two mechanical responses based on the atomistic scale core structure analyses will be presented in the following section: *Results and discussion*.

3. Results and discussion

3.1. Interrogation of dislocation core structure on glide along [001] (110) system in B2 NiTi

Though the GSFE curve shown in Fig. 1 (b) provides invaluable information about the glide energetics of {110} <001> dislocation in B2 NiTi, the spreading of screw dislocation cores can not be solely interrogated within the framework of GSFE curves. To that end, in order to establish a solid understanding of the slip characteristics entailing deviations from the Schmid law in B2 NiTi, we furthered the MS calculations to analyze the structure of screw dislocation cores. The displacement fields calculated for the stress-free configuration within the Eshelby-Stroh formalism is shown in Fig. 4 (a). For comparison, the resulting core structure obtained by relaxing the core structure is shown at Fig. 4 (b). Subsequent to the relaxation, displacements are concentrated on multiple $(\bar{1}10)$ planes suggesting the non-planar nature of the screw core in the stress-free configuration. This displacement configuration can be considered to be lowering the total energy of the structure by accommodating the large deformation inside the core over the multiple neighboring planes. Moreover, the absence of the multiple-fold fractional dislocation formation, unlike the non-planar core configuration of <111> dislocations, can be regarded as the most salient feature of the core structure.

3.2. The screw core structures under experimental stress states

3.2.1. <111> orientation

The experimental measurements indicate that there is a 42 MPa CRSS differential on the $[100](0\bar{1}1)$ glide system between the <111> oriented samples loaded under uniaxial tension and compression. Considering the two fold symmetry of <001> axis on {110} glide planes and the symmetric nature of the GSFE curve shown in Fig. 1 (b), the CRSS difference is not likely to

originate from the lattice structure but is a consequence of the interplay between the components of S tensor and the core displacements. The S tensor acting in $x_1 - x_2 - x_3$ frame is formed by the superposition of the normal stresses, S_{11}, S_{22}, and the glide shear stress S_{23} (with its symmetric component). In order to characterize the core structure under these components, we initially considered the contribution of the glide shear stress S_{23} on the core geometry in Fig. 5 (a) and then superposed the other S components upon the <111> tension and compression sample in Fig. 5 (b) and Fig. 5 (c) at a load step at which the Peierls stress corresponds to the half of the theoretical CRSS calculated from the modified Peierls-Nabarro analyses for each sample (as will be explained in the subsequent discussion). This examination is particularly explanatory to visualize the core configuration changes under different loading conditions.

Fig. 5 shows that the screw core configuration is highly sensitive to the applied loading conditions while transforming from the non-planar, compact stress-free configuration into a planar shape which exhibits the tendency of the core towards gliding. As can be seen in Fig. 5 (a), the core attains an almost planar shape under pure glide stress although, as can be seen in Fig. 5 (b) and (c), the planar extension of the core is different as a result of the different sense bi-axial loading $S_{11} - S_{22}$ acting under uniaxial tension and compression. The detailed consideration of the transformed elastic stiffness tensor, L_{ijkl}, indicates that there is no coupling components between the normal stress and the shear strain components in $x_1 - x_2 - x_3$ coordinate frame which can introduce shear strain from the normal stress components and change the planar extension of the core. On the other hand, it should be note that the relaxed deformation inside the core region exceeds the small-strain assumption of the linear elasticity. Therefore, the large deformation formulation of screw dislocations in anisotropic crystals (Willis, 1967) is required to be considered to quantify the coupling effects by utilizing the third order elastic constants, C_{ijklmn} (where i,j,k,l,m,n = 1,2,3). These third order constants can be extracted from the strain energy density formulation of Miller et al. (Miller and Phillips, 1996) for the potentials developed based on the Embedded Atom Method (Daw et al., 1993) as it is in our case. However, there is no experimental measurements available in the literature for the third order elastic constants of the binary alloy B2 NiTi for comparison, yet. Therefore, within the scope of this work, we will limit our attention to address the presence of the significant normal stress effects on the sessile-glissile transformation path of screw core structure in B2 NiTi which is reflected by the "non-unique" nature of the CRSS values.

3.2.2. <249> orientation

The experimental measurements indicate that slip initiates on $(\bar{1}10)$ glide system along the [001] direction under uniaxial tension and in the opposite sense under compression for the <249> oriented sample. Considering the similar arguments as discussed for the <111> orientation, the CRSS difference measured at the experiments (of 85 MPa) is a consequence of the core displacements interacting with the S tensor, which is composed of both glide, non-glide, normal and conjugate plane stress components.

Fig. 6(a)–(c) illustrates the core configuration of the screw dislocation with $\mathbf{b} = a\,[00\bar{1}]$ under a deviatoric stress state corresponding to the <249> compression sample at a load step at which the Peierls' stress corresponds to the half of theoretical CRSS level. As can be seen, the core displacements are extended mainly on the glide plane $(\bar{1}10)$. On the other hand, in Fig. 6(d) and (e) the screw dislocation with an opposite sign Burgers' vector under tension preserves its non-planar sessile structure with a 3 layered generalized stacking faults on $(\bar{1}10)$ planes. Considering the high slip resistance measured

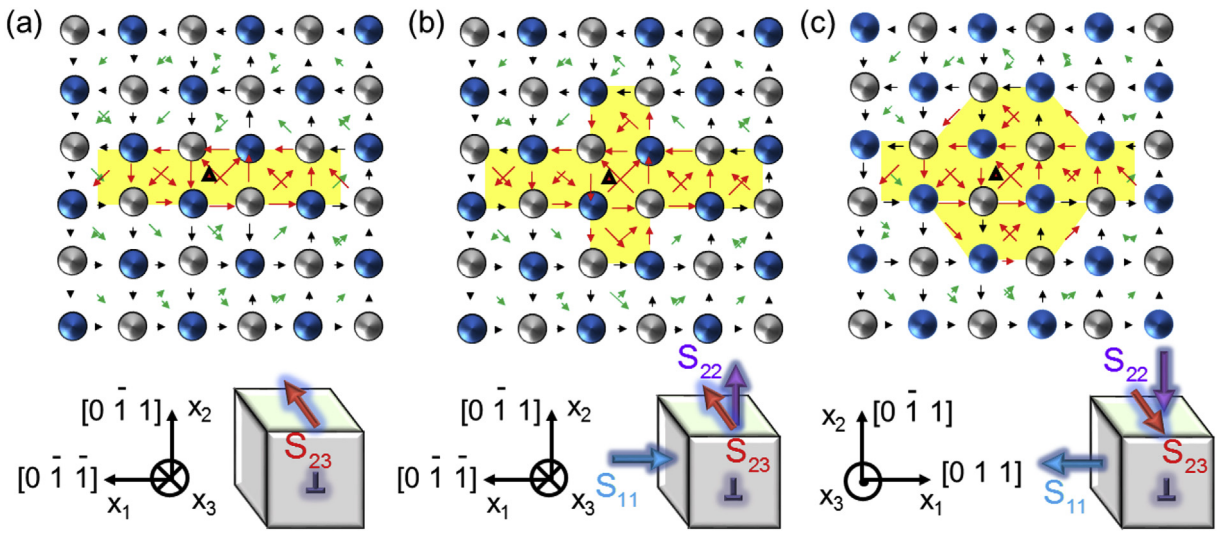

Fig. 5. **(a)** Shows the screw core structure under pure glide shear stress S_{23} only. **(b)** shows the screw dislocation core structure under a resultant deviatoric stress state corresponding to the <111> tension. **(c)** shows the screw dislocation corresponding to the stress state acting on the <111> compression sample. As can be seen, the normal stress components S_{11} and S_{22} affect the core structure transform into the glissile core configuration.

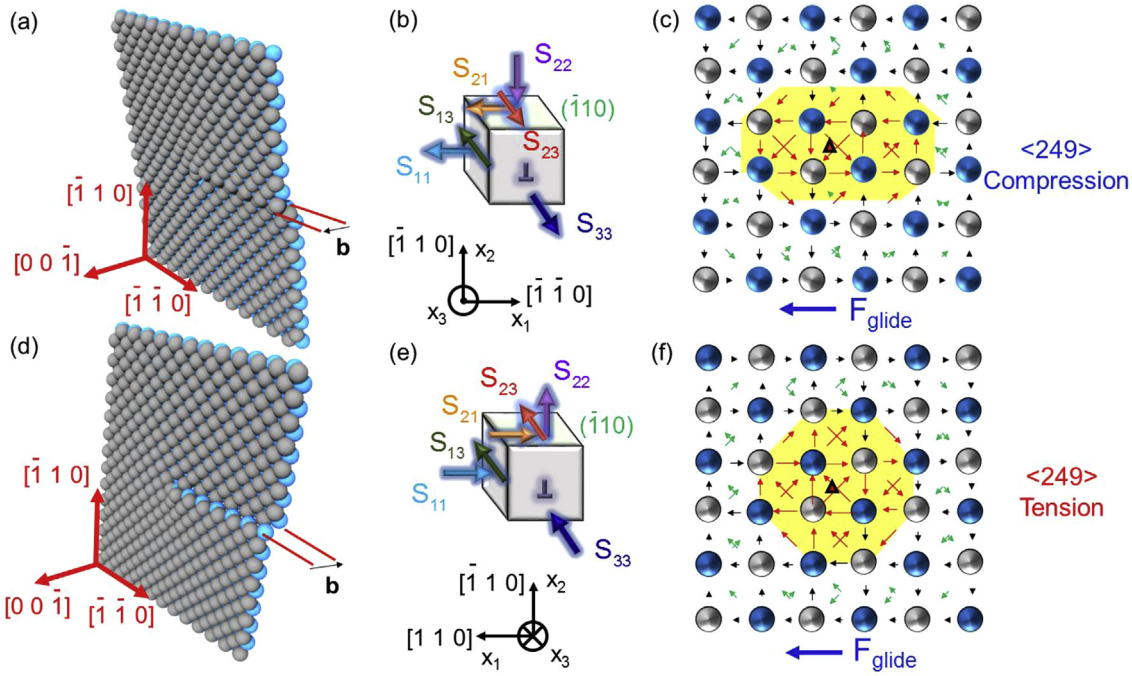

Fig. 6. **(a)** Shows the core region of the straight screw dislocation (Burgers' vector of a [001]) placed inside a designed B2 NiTi simulation box (150 × 150 × 3 Angstroms^3) utilizing Eshelby-Stroh formalism. **(b)** illustrates the applied deviatoric stress state corresponding to the uniaxial compression for the <249> compression sample **(c)** shows the relative atomic displacements parallel to [001], i.e.u_3, in the screw core region plotted utilizing DDMT under the applied stress state. As indicated by the relative displacements, in this configuration the core extends along the glide direction with the concerted effects of shear stress S_{23} and S_{21} in a planar fashion. **(d)** shows the core region of the straight screw dislocation with a Burger's vector of a [00$\bar{1}$]. **(e)** illustrates the applied deviatoric stress state corresponding to the <249> tension sample. **(f)** shows the core configuration under the applied stress state. In this configuration, the core structure is multi-layered. This is regarded to be a consequence of the opposing effect of S_{21} component to the glide shear stress S_{23}.

under uniaxial tension in the experiments, the multi-layered extension of the core in Fig. 6 (f) is expected to impart greater resistance against the glide motion. Therefore, higher CRSS values are to be applied to have the screw core structure attained a planar and glissile configuration under uniaxial tension.

A closer examination of the experimental measurements suggest that even though the CRSS level for <111> sample is greater under compression, for <249> sample the tensile loading imparts greater resistance against slip. The additional deviatoric stress components S_{33}, S_{21} and S_{13} (with their symmetric components) acting on the <249> oriented samples, compared to the <111> orientation, are expected to be responsible for this opposite trend. Previous atomistic scale calculations conducted on DO_3 ordered Fe_3Al suggests that non-glide shear stress components govern on the core shape in conjunction with the elastic coupling between non-glide shear stress and glide strain (Alkan and Sehitoglu, 2017a). A similar effect can be also present for B2 NiTi owing to the third order elastic constantsC_{ijklmn} as the coupling terms are zero in the second order elastic constants C_{ijkl} if transformed into the dislocation frame. This contention underlies the importance of the experimental measurement of C_{ijklmn} components in B2 NiTi as they are of significant importance in characterizing the large deformation on the ground of defect mechanics.

3. .3Theoretical prediction of CRSS values

The theoretical prediction of CRSS values to characterize the onset of slip necessitates a comprehensive description of the underlying mechanisms governing the transformation of the core structure from sessile into glissile configuration. In order to develop a theoretical slip model capable of explaining the non-Schmid behavior of CRSS values of B2 NiTi, we incorporate the modified Peierls-Nabarro approach to evaluate the Peierls' stress whose maximum value is equal to the theoretical CRSS in this context.

As an attempt to define the energy variation accompanying the core configuration changes, we will decompose the total energy, E^{tot}, into three primary terms: (i) the misfit energy, E^{mis}, (ii) the elastic energy, E^{e}, (iii) the applied work, W. These three terms are linked with E^{tot} as such (Lothe, 1992; Wang et al., 2014):

$$E^{tot} = E^{mis} + E^{e} - W \tag{7}$$

Among the three individual terms composing E^{tot}, the misfit energy E^{mis} stems from the atomic interaction across the glide plane and is directly linked with GSFE curve generated based on the disregistry function $u = f(x_1)$ as given by Eq. (8) in which x_1 is written in terms of integer multiples, i.e. m, of lattice translation vector, i.e. represented by the parameter m a, and the dislocation core center x_c (Joós et al., 1994; Tadmor and Miller, 2011):

$$E^{mis} = \sum_{m=-\infty}^{+\infty} \gamma(u) = \sum_{m=-\infty}^{+\infty} \gamma(f(x_1)) = \sum_{m=-\infty}^{+\infty} \gamma(f(ma + x_c))a \tag{8}$$

The concept of dislocation core center x_c conveys information about the shift of the dislocation line from the stress-free position as a result of applied loading. The translation of the core center is a mathematical manifestation of the sessile to glissile shape change of the core under an external stress state. A major point to discuss regarding the formulation in Eq. (8) is that the lattice discreteness introduced by the parameter 'ma ' bestows sensitivity to the series expression for the dislocation center position (Bulatov and Kaxiras, 1997; Nabarro, 1947a; Tadmor and Miller, 2011) which was not present in the original treatment of Peierls (1940).

The expression in Eq. (8) suggests that E^{mis} is governed by the GSFE profile on the glide plane. It is noteworthy to emphasize that the spatial variation of the GSFE is determined by the details of the $f(x_1)$ function which generates misfit stresses along the slip system equilibrating the corresponding applied stress component. This implies that the exact nature of the $f(x_1)$ variates in response to the increase in the applied loading state and intensity as a result of core shape changing to accommodate the deformation. In this work, in order to define $f(x_1)$ under a particular applied S tensor, we extracted the slip displacements, i.e. $u_3(x_1)$, on the glide plane from the MS simulation following the relaxation after each incremental load step. This approach allowed us to identify $f(x_1)$ throughout the loading path for each particular sample. Furthermore, as this particular disregistry distribution is ensured to satisfy the interatomic force equilibrium conditions owing to the relaxation, an accurate description of the dislocation core structure under the pertinent stress state is achieved.

On the other hand, to implement the required mathematics in an analytical fashion, we fitted the corresponding distribution of $u_3(x_1)$ displacements extracted from the MS simulation into the form, $f(x_1)$, expressed in Eq. (9) (Foreman et al., 1951; Kroupa and Lejček, 1972):

$$f(x_1) = \frac{b}{\pi}\left\{\tan^{-1}\frac{x_1 - x_c}{c\zeta} + (c-1)\zeta\frac{x_1 - x_c}{(c\zeta)^2 + (x_1 - x_c)^2}\right\} + \frac{b}{2} \tag{9}$$

ensuring the following boundary conditions in Eq. (10) are satisfied.

$$\lim_{x_1 \to -\infty} f(x_1) = b \quad ; \quad \lim_{x_1 \to \infty} f(x_1) = 0 \tag{10}$$

This fitting procedure enabled us to evaluate the coefficients c, ζ and x_c which are linked with the parameters depicting the core extent, i.e. the core width $c\zeta$ and the core center x_c at each load step. Moreover, based on Eq. (9), an implicit functional relationship between the core width $c\zeta$ and the dislocation center x_c is also established to be exploited in evaluating the theoretical CRSS value in the following discussion.

To illustrate the variation of $f(x_1)$ as the core structure gradually transforms from the sessile to glissile configuration, the core structure posited in the **<249> compression** sample is elaborated under increasing loading intensity. For this particular case, the explicit form of the applied deviatoric state is given as:

$$\mathbf{S} = \beta\begin{bmatrix} 0.31 & -1.26 & 0.63 \\ -1.26 & -0.88 & 1 \\ 0.63 & 1 & 0.57 \end{bmatrix} \text{MPa} \tag{11}$$

where β is the proportional loading coefficient.

The disregistry function, $f(x_1)$, in the sessile, stress-free configuration at $\beta = 0$ is plotted in Fig. 7(a) along with the core structure shown by DDMT in Fig. 7(b). In stress-free configuration, x_c is evaluated to be at the geometrical center of the lattice, i.e. $x_1 = 0$, and the core width $c\zeta$ is 5.52 Å. As β attains a value of 800, the core center shifts to $x_c = 1.0$ Angstrom and the core width increases to a value of 7.8 Å. These corresponding values suggest that the core structure extends over a wider region increasing its planarity and its center shifts in parallel to the acting glide force (also known as Peach-Koehler force), **F**, under the applied stress tensorS. The resulting $f(x_1)$ distribution is plotted also in Fig. 7(a) along with the corresponding core structure shown in Fig. 7(c). Finally, just before the onset of slip motion, at $\beta = 1300$, the corresponding core structure extends to a maximum width of 12 Å with a center value of $x_c = 1.4$ Angstroms. As can be seen in Fig. 7 (a) and (d), the core structure attains an almost planar configuration which facilitates the glide motion. Further increase in the stress introduces the translation of the dislocation by multiple lattice spacings. As a point of paramount importance, at this step, the applied glide stress component S_{23} attains a value of 1300 MPa which is higher than the experimentally measured CRSS, i.e. 178 MPa by more than 7 times. This order of difference in the stresses underlines the necessity of the modified Peierls-Nabarro analysis for the theoretical prediction of CRSS levels from the atomistic calculations.

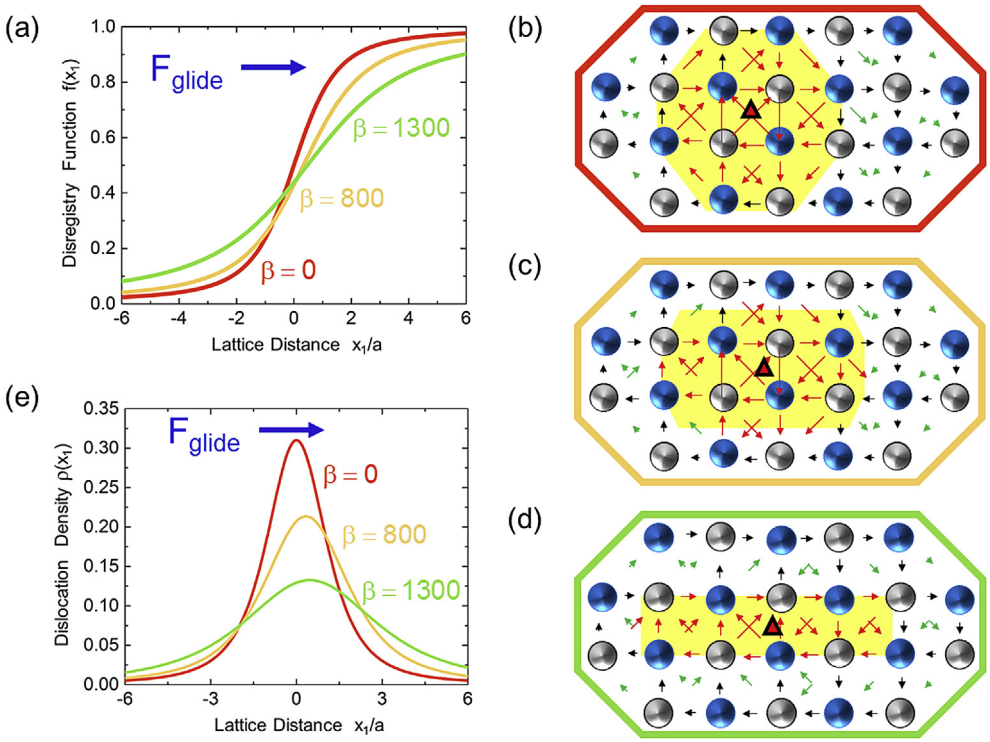

Fig. 7. Shows the variation of disregistry function $f(x_1)$ for the screw dislocation core structure under applied loading corresponding to the <249> compression sample with intensity $\beta = 0, 800, 1300$. The inset **(b)** shows the stress-free configuration illustrated also in Fig. 4. This configuration is sessile and the core displacements extend over three parallel $(\bar{1}10)$ planes. The core is symmetric with respect to the geometric center of the lattice ($x_c = 0$) as shown by the triangle symbol. The inset **(c)** shows the screw dislocation core configuration at $x_c = 1.0$. The core planarity increases under applied **S** tensor with $\beta = 800$. The inset **(d)** shows the glissile configuration just before the onset of slip at $\beta = 1300$. The planar structure of the core facilitates the glide under applied loading. **(e)** illustrates the dislocation density distribution $\rho(x_1)$ corresponding to $\beta = 0, 800, 1300$. As can be seen, the core extends with increasing β and finally attains a planar Burgers' vector distribution over multiple lattice spacing.

In order to further examine the core shape changes in response to the applied loading intensity, i.e.β, we utilized the infinitesimal dislocation distribution concept, $\rho(x_1)$, which is defined as the change in Burgers' vector between in the points x_1 and $x_1 + dx_1$ along the glide plane. Mathematically, $\rho(x_1)$ can be evaluated as the derivative of the disregistry function $f(x_1)$ with respect to x_1 as expressed in Eq. (12) ensuring the condition in Eq. (13) satisfied (Kroupa and Lejček, 1972).

$$\rho(x_1) \equiv \frac{df(x_1)}{dx_1} = \frac{b}{\pi}\zeta\frac{(x_1 - x_c)^2 + (2c-1)(c\zeta)^2}{\left((x - x_c)^2 + (c\zeta)^2\right)^2} \tag{12}$$

$$\int_{-\infty}^{+\infty} \rho(x_1)dx_1 = b \tag{13}$$

The introduction of $\rho(x_1)$ enables to characterize the differences in the core shapes of the screw dislocation posited in the <249> compression sample more explicitly under increasing load intensity. This point is illustrated in Fig. 7(e) for $\beta = 0, 800, 1300$. As the applied loading intensity increases, the peak value of $\rho(x_1)$ at $x_1 = x_c$ decreases considerably from 0.32b to 0.13b gradually. This depreciation in the density of the infinitesimal dislocation density indicates that the core extends into a planar shape in order to be able to attain a glissile configuration. The tendency of the dislocation core structure towards attaining a planar structure under increasing loading intensity, as illustrated in Fig. 7(c)–(e), facilitates the dislocation glide and decreases the theoretical CRSS values as will be demonstrated.

Revisiting the total energy description in Eq. (7), the term E^e stands for the line energy of the anisotropic screw dislocation and it is formulated as (Foreman, 1955; Lothe, 1992):

$$E^e = \frac{Kb^2}{4\pi}\ln\left(\frac{R}{c\zeta}\right) \tag{14}$$

In Eq. (14), K is the anisotropic energy factor which is equal to C_{44} for a screw dislocation with $\mathbf{b} = a[001]$ in B2 lattice structure. The R term is the outer cut-off radius and it is taken as a constant which is equal to 500 b throughout the calculations. As can be seen, both E^{mis} and E^{e} terms are dependent on the core width. This attribute in E^{e} complies with the original treatments of Eshelby et al. (1953) and Foreman (1955) within the framework of anisotropic linear elasticity as they excluded the energetic contribution of the volume in which core structure resides, from their analyses. At this point, it is to be noted that the elastic line energy definition can be extended to include the discrete lattice structure inside the screw core region (Esterling, 1978; Maradudin, 1959). However, as we utilize the interatomic force definitions already incorporated inside the misfit energy term E^{mis}, only the long range elastic energy is considered under E^{e} term.

The W term in Eq. (7) represents the work done by the applied stresses during the glide of a unit length screw dislocation on the glide plane. In addition to the glide stress S_{23}, the normal, S_{22}, and non-glide shear, S_{21}, stress components acting on the slip plane also contribute to the work done as a result of the core relaxation equilibrating the interatomic forces within the proximity of dislocation core region. Therefore, the applied work is given by the expression in Eq. (15) (Lu et al., 2000; Peach and Koehler, 1950) in which each of the displacement components, i.e. u_1, u_2 and u_3, are functions of both the external deviatoric stress tensor,S and the spatial coordinates.

$$W = S_{23}\int_{-75}^{+75} x_1 \underbrace{\frac{\partial u_3(\mathbf{S})}{\partial x_1}}_{\rho(x_1)} dx_1 + S_{22}\int_{-75}^{+75} x_1 \frac{\partial u_2(\mathbf{S})}{\partial x_1} dx_1 + S_{21}\int_{-75}^{+75} x_1 \frac{\partial u_1(\mathbf{S})}{\partial x_1} dx_1 \tag{15}$$

The theoretical CRSS levels for each sample can be evaluated based on the normalized (with respect to b) maximum gradient of E^{tot} with respect to the disregistry $u = \alpha b$ $(0 \le \alpha \le 1)$, i.e. max. Peierls' stress, as follows (Christian and Vítek, 1970):

$$\mathrm{CRSS} = \max\left(\frac{1}{b^2}\frac{\partial E^{tot}}{\partial \alpha}\right) \tag{16}$$

The resulting theoretical CRSS values for the screw dislocations corresponding to the <111>, <349>, <5 8 18>, <249>, <259>, <148>, <188> and <011> oriented samples under uniaxial tension and compression are plotted in Fig. 8. The experimentally measured values are also included for comparison purposes. The experiments are conducted in the B2 regime and the onset of slip is detected with digital image correlation. To ensure no transformation or twinning developed, the samples were checked with EBSD (Electron Back Scatter Diffraction). As can be seen, the theoretical results show close correspondence with the experimental measurements exhibiting both crystal anisotropy and tension-compression asymmetry.

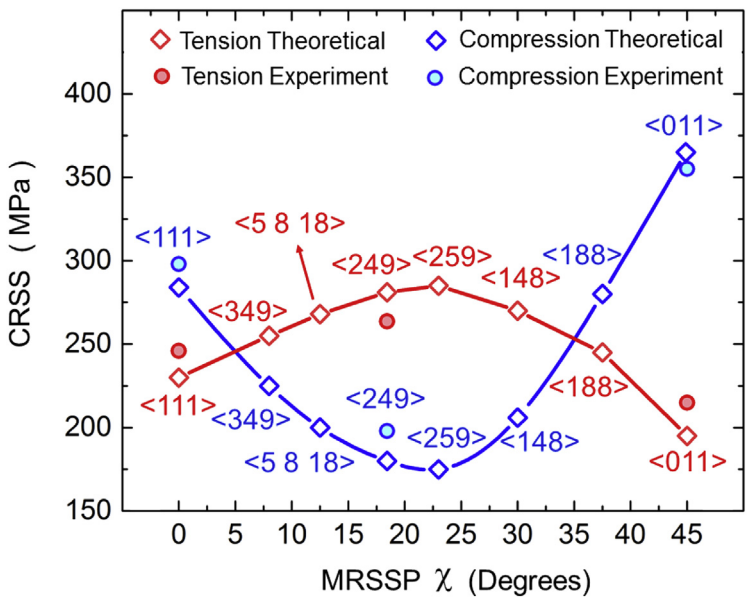

Fig. 8. The CRSS as a function of the characteristic angle χ showing considerable tension-compression asymmetry and crystal orientation dependence. The lines are placed to guide the eye.

Table 2
Tabulates the dislocation center, x_c, the free parameterζ and the core width $c\zeta$ values calculated under uniaxial loading along different crystallographic directions just before the glide motion such that x_c varies between 1.38 and 1.44 Å.

Loading Sense	x_c (Angstrom)	ζ (Angstrom)	$c\zeta$ (Angstrom)
Stress-Free	0	1.15	5.52
<111> T	1.39	3.09	10.65
<111> C	1.39	2.14	8.95
<349> T	1.43	2.69	10.04
<349> C	1.41	3.24	10.91
<5 8 18> T	1.42	2.51	9.81
<5 8 18> C	1.43	3.69	11.44
<249> T	1.42	2.22	9.10
<249> C	1.40	4.00	12.00
<259> T	1.41	2.05	8.71
<259> C	1.42	3.84	11.73
<148> T	1.40	2.39	9.67
<148> C	1.41	3.41	11.07
<188> T	1.43	2.87	10.23
<188>C	1.42	2.31	9.40
<011> T	1.38	3.92	11.86
<011> C	1.44	1.86	8.18

Below Table 2 shows the variation of the parameters ζ and $c\zeta$ based on the crystal orientation and the loading sense (tension or compression) just before the glide motion. As can be seen, both parameters are highly sensitive to the loading sense and varies also significantly in response to the orientation change. It is worth emphasizing that the greater the planar extension of the relative displacements within the core region of the screw dislocations, as can be seen in Figs. 5 and 6, the greater value of the parameters ζ and $c\zeta$. Therefore, the value of the core width parameter$c\zeta$ can be interpreted as an indicator of the planarity of the dislocation core structure.

The comparison between the core width values in Table 2 and the CRSS values in Fig. 8 suggests that the core width variation accompanying the core shape change is of fundamental importance on the CRSS levels. The extension of the core width $c\zeta$ accompanied with the drop in the peak value of dislocation density, $\rho(x_c) = (b/\pi)(2c-1)/c^2\,\zeta$, promotes a planar core configuration decreasing the lattice glide resistance. The close examination of dislocation core width and center values along with the theoretical and experimental CRSS values addresses that glide of a dislocation inside a discrete lattice structure is not an abrupt phenomenon but a process accompanied with the gradual changes in the core shape and center under the applied loading. Therefore, the CRSS values couple with the applied stress components and do not exhibit a unique value for a particular glide system as Schmid Law predicts.

One of the important points to discuss in assessing the theoretical work presented in this paper with the experimental measurements is that the finite temperature (293 K) in which the experiments are conducted might introduce additional mechanisms such as thermally activated kink-pair formation or cross-slip of the glissile dislocations. On the other hand, these mechanisms generally tend to smear-out the existing non-Schmid effects associated with the dislocation core shape on the plastic yielding around room temperature (293 K) as observed in several bcc structured pure metals or alloy systems such as Nb (Mitchell et al., 1963), Ta (Sherwood et al., 1967), Fe (Keh and Nakada, 1967; Patra et al., 2014), CuZn (Hanada et al., 1975). On the other hand, for B2 NiTi, the core effects on the plastic deformation persist even at finite temperatures. At this stage, it is crucial to point out that the prevalence of the non-Schmid effects at 293 K is closely related to the strength of the anisotropic bonding structure prevalent in B2 NiTi (Eibler et al., 1987; Hu et al., 2006). Similar behavior has been also observed for iron aluminides (Alkan and Sehitoglu, 2017a; Yoo and Fu, 1991). These theoretical and experimental evidence also present a motivation for interrogating the plastic glide behavior of other shape memory alloys as these materials are known to exhibit strongly order dependent mechanical behavior owing to their complicated anisotropic bonding structure.

3.4. Characterization of yielding in B2 NiTi

The influence of the dislocation core is not confined to atomistic scale but also extends to the macroscopic plastic behavior of B2 NiTi. Although numerous studies have focused on proposing transformation criteria for NiTi (Gall et al., 1999; Patoor et al., 1995; Saleeb et al., 2011; Taillard et al., 2006), no such effort has been yet attributed to identify the onset of slip in the literature other than the conventional Schmid Law which we show herein to deviate considerably from the experimental theoretical values. Considering the paramount importance of the slip in functional performance of NiTi, we extended our analyses to characterize the onset of yielding by means of the applied deviatoric stress tensor components. To that end, we propose a generalized yield criterion (Lim et al., 2013; Patra et al., 2014; Qin and Bassani, 1992) as expressed in Eq. (17) based on the theoretical and experimental measurements. For this purpose, we utilized S tensor components corresponding to the <111>, <349>, <5 8 18>, <249>, <259>, <148>, <188> and <011> oriented samples under uniaxial tension and compression. As any deviatoric tensor can be uniquely defined based on five independent components, we utilized the S tensor components of S_{11}, S_{22}, S_{21}, S_{13} and S_{23}, i.e. CRSS.

Table 3
Tabulates the values of the resulting for the parameters τ_{cr}, a_1, a_2, a_3, a_4 utilized in Eq. (9).

τ_{cr} (MPa)	a_1	a_2	a_3	a_4
240	0.14	0.11	−0.19	0.22

Table 4
The CRSS values calculated from the generalized yield criterion and the modified Peierls-Nabarro method are tabulated along with the experimental measurements. All the tabulated values are in units of MPa.

	Generalized Yield Criterion (Eq. (9), MPa)	Modified Peierls-Nabarro (This study, MPa)	Experimental Measurement (This study, MPa)
<111> Tension	234	230	246
<111> Compression	274	283	284
<349> Tension	268	255	-
<349> Compression	219	225	-
<5 8 18> Tension	272	268	-
<5 8 18> Compression	213	200	-
<249> Tension	275	281	262
<249> Compression	181	180	177
<259> Tension	276	285	-
<259> Compression	187	195	-
<148> Compression	205	206	-
<148> Tension	261	270	-
<188> Compression	282	280	-
<188> Tension	237	245	-
<011> Compression	361	365	334
<011> Tension	212	195	214

$$\tau_{cr} = \mathrm{CRSS} + a_1 S_{11} + a_2 S_{22} + a_3 S_{21} + a_4 S_{13} \tag{17}$$

The parameters τ_{cr}, a_1, a_2, a_3 and a_4 are evaluated from the S tensor components via a multi-variable linear regression analysis. The resulting values of these parameters are tabulated in Table 3.

As can be seen in Table 4, the CRSS values predicted by the generalized yielding criterion, Eq. (17), based on the deviatoric stress state are in close agreement with the theoretical results calculated within the modified Peierls-Nabarro framework and the experimental measurements. The close correspondence of the different approaches addresses that in order to characterize the yielding behavior in B2 NiTi, both normal, S_{11}, S_{22} and shear character, S_{12} and S_{13}, stress components should also be considered with the resolved shear stress acting along the glide direction, i.e. S_{23}. This stems from the fact that as the core structure gradually transforms into a planar, glissile shape from a sessile configuration, the stress components other than the glide shear stress contributes to the displacement field inside the core (Gröger and Vitek, 2013; Paidar et al., 1984). Therefore, the tensor S should be considered with its each independent component unlike the classical approach focusing only on the glide shear stress in order to characterize the onset of slip in B2 NiTi.

In order to examine the yielding behavior of single crystalline B2 NiTi specimens with an arbitrary uniaxial loading orientation, we revisit the concept of Schmid factor and modify it for the generalized yielding criterion expressed in Eq. (17). Based on conventional Schmid Law, the CRSS value can be calculated from the inner product of the applied deviatoric stress **S** with the Schmid tensor **P** as follows in Eq. (18):

$$\mathrm{CRSS} = \mathbf{S} : \mathbf{P} \tag{18}$$

where (:) is the tensor inner-product operator. The Schmid tensor **P** depends on the single crystal loading axis and can be evaluated by utilizing the unit glide plane normal **n** and the unit slip direction **m** vectors of the active glide system in the same coordinate frame as **S** tensor. The formulation for **P** is expressed in Eq. (19) where ⊗ is the tensor outer-product operator.

$$\mathbf{P} = \frac{1}{2}(\mathbf{m} \otimes \mathbf{n} + \mathbf{n} \otimes \mathbf{m}) \tag{19}$$

On the other hand, the onset of yield in B2 NiTi can be predicted based on Eq. (20) within the framework of the generalized yield criterion introduced.

$$\tau_{cr} = \mathbf{S} : \mathbf{P_{mod}} \tag{20}$$

In Eq. (21), the modified Schmid tensor P_{mod} is defined as following:

$$\mathbf{P_{mod}} = \mathbf{P} + a_1(\mathbf{n}x\mathbf{m}) \otimes (\mathbf{m}x\mathbf{n}) + a_2\mathbf{n} \otimes \mathbf{n} + a_3\mathbf{n} \otimes (\mathbf{n}x\mathbf{m}) + a_4(\mathbf{n}x\mathbf{m}) \otimes \mathbf{m} \tag{21}$$

where (x) stands for the vector cross-product operator. These tensorial definitions of $\mathbf{P}$ and $\mathbf{P_{mod}}$ are useful from an engineering perspective as they can be utilized to calculate the scalar projection factors P and P_{mod} along with an arbitrary unit vector $\mathbf{v}$ set parallel to the crystallographic loading direction (Weinberger et al., 2012) as follows:

$$P = \mathbf{v} \bullet \mathbf{P} : \mathbf{v} \tag{22}$$

$$P_{mod} = \mathbf{v} \bullet \mathbf{P_{mod}} : \mathbf{v} \tag{23}$$

In Eq. (22) and (23), P and P_{mod} are the denoted as Schmid factor and the modified Schmid factor respectively. These two projection factors can be demonstrated to quantify the onset of slip for a single crystal with an arbitrary $\mathbf{v}$ vector as slip initiates on a candidate glide system when the corresponding factor attains the maximum value depending on the yield criterion utilized, i.e. Eq. (18) or Eq. (20). Based on this rationale, the distribution of P and P_{mod} on the stereographic triangle conveys the critical information of the single crystal orientations which will yield earliest under uniaxial loading, i.e. the orientations with max (P) and max (P_{mod}).

As can be seen in Fig. 9, the modified Schmid factor, P_{mod}, in B2 NiTi exhibits significant tension-compression asymmetry manifested by the localization of the maximum value of the contours in the central zone for the uniaxial compression, in Fig. 9 (a), and within the neighborhood of the [111]-[011] line for the uniaxial tension, in Fig. 9 (b). The conventional Schmid law is not sufficient to distinguish tension-compression asymmetry as it predicts that the single crystals with uniaxial loading direction parallel to [111] yields earlier compared to the other orientations under both tension and compression, i.e. shown in Fig. 9 (c). As B2 NiTi yielding behavior deviates from the Schmid law and exhibits tension-compression asymmetry, the use of P_{mod} factor is of paramount importance for an accurate prediction of plastic yielding.

3.5. Ramifications of the results in the shape memory field –internal stresses, hysteresis and fatigue effects

As stated earlier in the introduction of the paper, the dislocation mediated slip produces redistribution of internal stresses. The local slip at transforming interfaces results in relaxation of internal stresses and activation of transformation in other domains of the specimen during subsequent transformation cycles (Gall et al., 2001). Without the understanding of the propensity of slip in different orientations, it would be difficult to understand how such a rearrangement in internal stress would be observed. For example the 011 grains slip readily in tension but rather strong in compression based on the results presented. Such anisotropy at the local level could generate large internal stresses upon cycling. Once the internal stresses are introduced, the transformation lattice correspondences that are favored are selected, and upon subsequent thermal cycling the material response will undergo transient changes. To ensure recoverability at microscale and upon repeated cycles the

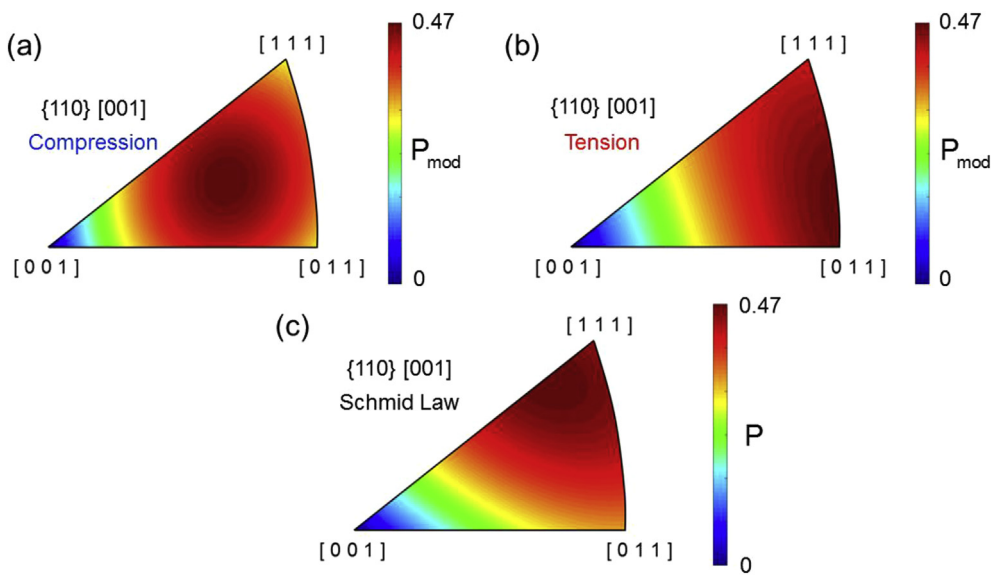

Fig. 9. Shows the distribution of modified Schmid factor, P_{mod}, in [001]-[011]-[111] stereographic triangle based on the deviatoric stress states corresponding to the CRSS values of modified Peierls-Nabarro calculations: (a) under uniaxial compression, (b) under uniaxial tension. For comparison purposes, P factor distribution for the conventional Schmid law is also plotted in (c). It is to be noted P value is same for both tension and compression. As can be seen, there is significant degree of tension - compression asymmetry at the onset of plastic glide in B2 NiTi.

external stress levels can not far exceed the local slip stress. In that case, the degradation in functionality can develop negatively impacting the shape memory response (Chowdhury and Sehitoglu, 2016).

The results may partially explain the reason for larger accumulation of residual strains observed in compression such as in the [148] orientation (Gall et al., 1998). No one has been able to explain it based on scientific grounds so far. As shown in Fig. 8, the CRSS in compression falls below the corresponding tensile CRSS levels in the [148] case. Therefore, the slip stress upon transformation can more readily be reached in compression compared to tension adversely affecting the reversibility. It has been proposed that the development of dislocations at the austenite-martensite interfaces will change the internal stresses and shift the active martensite variants to other grains (domains) (Sedmák et al., 2015). Consequently, with continuous cycling and increase in dislocation density, the matrix slip resistance increases and ultimately approaches a saturation state. The stress hysteresis loop will also reach a steady state (Miyazaki et al., 1986; Sehitoglu et al., 2001; Strnadel et al., 1995; Zaki et al., 2016). The high asymmetry of slip (shown in this work) will further modify the evolution of internal stresses and the hysteresis response with cycles. Similarly, in isobaric experiments with thermal cycling, the initial accumulation of residual strains with cycles is followed by saturation of the loops leading to shakedown similar to that observed in metal plasticity (Miller and Lagoudas, 2000). Therefore, in both isothermal superelasticity and isobaric shape memory experiments discussed above, the non-Schmid slip behavior is expected to modify the transformation response by creating additional internal stresses. To that end, future constitutive behavior descriptions must account for the non-Schmid effects and alteration of internal stresses.

The development of high internal stresses can be deleterious to fatigue response. Because fatigue crack nucleation will develop when the energy stored reaches a critical value in persistent slip bands, it would favor grains and domains that carry high internal stresses (Chowdhury and Sehitoglu, 2017a). Therefore large levels of internal inhomogeneity could result in localization and onset of crack nucleation earlier than expected. For fatigue considerations, crystal plasticity formulations that typically assume Schmid law need to be revised. This has implications in the response in terms of fatigue crack growth characteristics because the slip zone immediately ahead of the crack tip exists whether the remaining body undergoes reversible transformation. Irreversible slip at crack tips can promote accumulation of strains, and favorable conditions for accelerated crack growth.

Apart from the factors discussed above, the high asymmetry of the slip in shape memory alloys has implications in processing of these alloys in the austenitic phase. Even though the non-Schmid effects are believed to be confined to low temperatures in traditional bcc alloys, the situation differs in bcc ordered alloys. Clearly, in SMAs this effect extends to finite temperatures where phenomenon such as aging, deformation processing may take place. A better understanding of the permanent deformation behavior under different stress states would assist in predicting the shape setting operations. Furthermore, in engineering applications such as bending and twisting, the stress states are complex which also necessitate a rigorous description of the yield surface which is accomplished in this paper.

4. Conclusions

Following conclusions are drawn from this work:

(1) The core structure of a screw dislocation on {110} <001> glide system family in NiTi is evaluated by utilizing the Eshelby-Stroh anisotropic formulation in conjunction with molecular statics. The core displacements extended over three {110} layers in the stress-free configuration while spreading of the core developed upon applied stress.
(2) The core shape of the screw dislocation exhibits variations under varying applied stress tensor components. It has been observed that the non-glide shear stress acting parallel/opposite sense to the applied glide force facilitates/hardens the glide motion. It is shown that the CRSS values are closely linked with the planar extent of the core displacement field.
(3) A modified Peierls-Nabarro formulation has been established which can successfully capture both crystal orientation and tension-compression asymmetry observed in the experimental CRSS values in a quantitative fashion. Mathematically, it has been shown that the core width affecting the disregistry inside the dislocation core is decisive on the CRSS values.
(4) The results show clearly why <111> oriented crystals are favored in shape memory. This is because our calculations and experiments clearly address that this orientation exhibits higher slip resistance than expected based on Schmid factor considerations.
(5) The results also point to the high slip resistance of <148> and <249> orientations in tension. In fact, the early experimental results in tension have already pointed to the superior shape memory response of single crystals tested in these orientations.

Acknowledgements

The work is supported by Nyquist Chair funds.

Appendix A

In this study, the many-body potential constructed for the binary NiTi alloy is utilized (Chowdhury et al., 2016; Ren and Sehitoglu, 2016). In this framework, the potential energy, E^{pot} expressed in Eq. (A.1), is composed of interatomic pair-

interaction potential, $\phi_{t_i t_j}(r_i - r_j)$, (defined with respect to the relative position vector between atom i and atom j: $r_i - r_j$) and the embedding energy function, $F_{t_i t_j}\left(\rho^e_{t_i t_j}(r_i - r_j)\right)$, which represents the contribution of host electron density $\rho^e_{t_i t_j}(r_i - r_j)$. The subscript $t_k (k = 1,2)$ represents the atom element type, i.e. either Ni or Ti along with N = 2.

$$E^{pot} = \sum_{i=1}^{N-1} \sum_{j=i+1}^{N} \phi_{t_i t_j}(r_i - r_j) + F_{t_i t_j}\left(\rho^e_{t_i t_j}(r_i - r_j)\right) \tag{A.1}$$

The electron density term, $\rho^e_{t_i t_j}$, is simply the superposition of the valence electron clouds from all other atoms. The current potential adopts the existing potentials of Ni (Mishin, 2004) and Ti (Zope and Mishin, 2003) along with the cross-interaction terms of $\rho^e_{t_i t_j}$ and $\phi_{t_i t_j}$ from the cubic spline form given in Eqs. (A.2) -(A.3) as follows:

$$\rho^e(r) = \sum_{i}^{N} a_i (r_i - r)^3 H(r_i - r) \tag{A.2}$$

$$\phi(r) = \sum_{i=1}^{N} c_i (r_i - r)^3 H(r_i - r) \tag{A.3}$$

where N, r_i represent the number of knots, the knot position vector for a fixed r vector respectively along with the to-be determined coefficients a_i and c_i. H function is the Heaviside step function which is equal to 0 for $r_i < r$ and equal to 1 for $r_i \geq r$. In the calculations conducted to construct the potential, the maximum value of r_i is set equal to the cut-off radius R_c which is equal to 0.52 nm. These cross-interaction terms are fitted by conducting ab-initio simulations within framework of Density Functional Theory by Quantum Espresso software (Paolo et al., 2009). The ab-initio simulations are conducted by using ultra-soft pseudopotentials plus generalized gradient approximation for energy versus volume relation of (i) the crystal structures of B2, B19′, B19, BCO (body-centered orthogonal) and (ii) hypothetical compounds of B1-NiTi, $L1_2$-Ni_3Ti, $L1_2$-$NiTi_3$. Generalized gradient approximation can capture both the electron density and its gradient at a given point r and enables to calculate lattice constants and elastic coefficients with high precision (Paier et al., 2006). On the other hand, ultra-soft pseudopotentials enable to get improved accuracy in representing the valence pseudo-wave functions for transition metal systems within a small cut-off distance (Vanderbilt, 1990).

The fitting procedure introduced in Eqs. (A.2)-(A.3) is performed by minimizing the objective function Z expressed in Eq. (A.4) for the fitting constants a_i and c_i through the use of downhill simplex minimization (Nelder-Mead) method (Avriel, 2003).

$$Z = \sum_{i=1}^{N} w_i [Y_i(r, a_i) - Y_{i0}]^2 + \sum_{i=1}^{N} w_i [Y_i(r, c_i) - Y_{i0}]^2 \tag{A.4}$$

In Eq. (A.4), w_i is the fitting weight of the different terms, $Y_i(r, a_i)$ and $Y_i(r, c_i)$ are the adjustable fitting value for the constants a_i and c_i respectively. The term Y_{i0} represents the target value calculated by the ab-initio simulation. The resulting values for the fitting constants a_i and c_i are reported in reference (Ren and Sehitoglu, 2016). Below, Table A.1 tabulates the equilibrium volume per atom per unit cell (V_0) and the lattice constant (a) corresponding to B2 structure obtained from the potential in comparison with the experimental measurements. Moreover, the second order elastic stiffness constants of B2 NiTi (in Voigt notation) are also compared with the experimental findings of (Mercier et al., 1980) in Table A.2.

Table A.1
Tabulates the volume V_0(Angstrom^3), the lattice constant a (Angstrom) for B2 ordered NiTi in comparison with experimental measurements from the corresponding references.

	V_0 (Angstrom^3)	a (Angstrom)
B2 (**This potential**)	27.561	3.021
B2 Exp. (Sittner et al., 2003)	27.339	3.013

Table A.2
Tabulates the elastic stiffness tensor components C_{11}, C_{12} and C_{44} evaluated from the potential utilized for B2 NiTi. The experimental measurements are also included for comparison purposes.

	C_{11} (GPa)	C_{12} (GPa)	C_{44} (GPa)
Potential (**this study**)	146	122	35
Experimental (Mercier et al., 1980)	162	129	35

References

Alexander, S., 2010. Visualization and analysis of atomistic simulation data with OVITO–the Open Visualization Tool. Model. Simul. Mater. Sci. Eng. 18, 015012.
Alkan, S., Sehitoglu, H., 2017a. Non-Schmid response of Fe3Al: the twin-antitwin slip asymmetry and non-glide shear stress effects. Acta Mater. 125, 550–566.
Alkan, S., Sehitoglu, H., 2017b. Giant non-Schmid effect in NiTi. Extrem. Mech. Lett. 15, 38–43.
Avriel, M., 2003. Nonlinear Programming: Analysis and Methods. Courier Corporation.
Benafan, O., Noebe, R.D., Padula Ii, S.A., Garg, A., Clausen, B., Vogel, S., Vaidyanathan, R., 2013. Temperature dependent deformation of the B2 austenite phase of a NiTi shape memory alloy. Int. J. Plasticity 51, 103–121.
Bulatov, V.V., Kaxiras, E., 1997. Semidiscrete variational peierls framework for dislocation core properties. Phys. Rev. Lett. 78, 4221–4224.
Chowdhury, P., Sehitoglu, H., 2016. Significance of slip propensity determination in shape memory alloys. Scr. Mater. 119, 82–87.
Chowdhury, P., Sehitoglu, H., 2017a. Deformation physics of shape memory alloys – fundamentals at atomistic frontier. Prog. Mater. Sci. 88, 49–88.
Chowdhury, P., Sehitoglu, H., 2017b. A revisit to atomistic rationale for slip in shape memory alloys. Prog. Mater. Sci. 85, 1–42.
Chowdhury, P., Patriarca, L., Ren, G., Sehitoglu, H., 2016. Molecular dynamics modeling of NiTi superelasticity in presence of nanoprecipitates. Int. J. Plasticity 81, 152–167.
Christian, J.W., 1983. Some surprising features of the plastic deformation of body-centered cubic metals and alloys. Metallurgical Trans. A Phys. Metallurgy Mater. Sci. 14A, 1237.
Christian, J.W., Vítek, V., 1970. Dislocations and stacking faults. Rep. Prog. Phys. 33, 307.
Daw, M.S., Foiles, S.M., Baskes, M.I., 1993. The embedded-atom method: a review of theory and applications. Mater. Sci. Rep. 9, 251–310.
Duesbery, M.S., 1984. On non-glide stresses and their influence on the screw dislocation core in body-centred cubic metals ii. The core structure. Proc. R. Soc. Lond. Ser. A, Math. Phys. Sci. 392, 175–197.
Duesbery, M.S., 1989. The dislocation core and plasticity. In: Nabarro, F.R.N. (Ed.), Dislocations in Solids. Elsevier Science Publishers B.V., Netherlands, pp. 67–173.
Duesbery, M.S., Vitek, V., 1998. Plastic anisotropy in b.c.c. transition metals. Acta Mater. 46, 1481–1492.
Duesbery, M.S., Vitek, V., Bowen, D.K., 1973. The effect of shear stress on the screw dislocation core structure in body-centred cubic lattices. Proc. R. Soc. Lond. A. Math. Phys. Sci. 332, 85.
Eibler, R., Redinger, J., Neckel, A., 1987. Electronic structure, chemical bonding and spectral properties of the intermetallic compounds FeTi, CoTi and NiTi. J. Phys. F Metal Phys. 17, 1533.
Eshelby, J.D., Read, W.T., Shockley, W., 1953. Anisotropic elasticity with applications to dislocation theory. Acta Metall. 1, 251–259.
Esterling, D.M., 1978. Modified lattice-statics approach to dislocation calculations I. Formalism. J. Appl. Phys. 49, 3954–3959.
Ezaz, T., Wang, J., Sehitoglu, H., Maier, H.J., 2013. Plastic deformation of NiTi shape memory alloys. Acta Mater. 61, 67–78.
Finnis, M.W., Sinclair, J.E., 1984. A simple empirical N-body potential for transition metals. Philos. Mag. A 50, 45–55.
Foreman, A.J.E., 1955. Dislocation energies in anisotropic crystals. Acta Metall. 3, 322–330.
Foreman, A.J., Jaswon, M.A., Wood, J.K., 1951. Factors controlling dislocation widths. Proc. Phys. Soc. Sect. A 64, 156.
Gall, K., Sehitoglu, H., Chumlyakov, Y.I., Kireeva, L.V., 1998. Pseudoelastic cyclic stress-strain response of over-aged single crystal Ti-50.8at%Ni. Scr. Mater. 40, 7.
Gall, K., Sehitoglu, H., Chumlyakov, Y.I., Kireeva, I.V., 1999. Tension–compression asymmetry of the stress–strain response in aged single crystal and polycrystalline NiTi. Acta Mater. 47, 1203–1217.
Gall, K., Sehitoglu, H., Anderson, R., Karaman, I., Chumlyakov, Y.I., Kireeva, I.V., 2001. On the mechanical behavior of single crystal NiTi shape memory alloys and related polycrystalline phenomenon. Mater. Sci. Eng. A 317, 85–92.
Gröger, R., Vitek, V., 2013. Stress dependence of the Peierls barrier of $1/2\langle 1\,1\,1\rangle$ screw dislocations in bcc metals. Acta Mater. 61, 6362–6371.
Gröger, R., Bailey, A.G., Vitek, V., 2008a. Multiscale modeling of plastic deformation of molybdenum and tungsten: I. Atomistic studies of the core structure and glide of $1/2\langle 1\,1\,1\rangle$ screw dislocations at 0 K. Acta Mater. 56, 5401–5411.
Gröger, R., Racherla, V., Bassani, J.L., Vitek, V., 2008b. Multiscale modeling of plastic deformation of molybdenum and tungsten: II. Yield criterion for single crystals based on atomistic studies of glide of screw dislocations. Acta Mater. 56, 5412–5425.
Hamilton, R.F., Sehitoglu, H., Chumlyakov, Y., Maier, H.J., 2004. Stress dependence of the hysteresis in single crystal NiTi alloys. Acta Mater. 52, 3383.
Hanada, S., Mohri, M., Izumi, O., 1975. Plasticity of β-brass single crystals at low temperatures. Trans. Jpn. Inst. Metals 16, 453–461.
Hu, Y.-f., Deng, W., Hao, W.E.N.b., Yue, L., Huang, L., Huang, Y.-y., Xiong, L.-y., 2006. Microdefects and electron densities in NiTi shape memory alloys studied by positron annihilation. Trans. Nonferrous Metals Soc. China 16, 1259–1262.
Joós, B., Ren, Q., Duesbery, M.S., 1994. Peierls-Nabarro model of dislocations in silicon with generalized stacking-fault restoring forces. Phys. Rev. B 50, 5890–5898.
Keh, A.S., Nakada, Y., 1967. Plasticity of iron single crystals. Can. J. Phys. 45, 1101–1120.
Kroupa, F., Lejček, L., 1972. Splitting of dislocations in the Peierls-Nabarro model. Czechoslov. J. Phys. B 22, 813–825.
Lim, H., Weinberger, C.R., Battaile, C.C., Buchheit, T.E., 2013. Application of generalized non-Schmid yield law to low-temperature plasticity in bcc transition metals. Model. Simul. Mater. Sci. Eng. 21, 045015.
Lothe, J.P.H.J., 1992. Theory of Dislocations, 2 ed. Krieger Pub. Co.
Lu, G., Kioussis, N., Bulatov, V.V., Kaxiras, E., 2000. The peierls-nabarro model revisited. Philos. Mag. Lett. 80, 675–682.
Maradudin, A.A., 1959. Screw dislocations and discrete elastic theory. J. Phys. Chem. Solids 9, 1–20.
Mendelev, M.I., Sordelet, D.J., Kramer, M.J., 2007. Using atomistic computer simulations to analyze x-ray diffraction data from metallic glasses. J. Appl. Phys. 102, 043501.
Mercier, O., Melton, K.N., Gremaud, G., Hägi, J., 1980. Single-crystal elastic constants of the equiatomic NiTi alloy near the martensitic transformation. J. Appl. Phys. 51, 1833–1834.
Miller, D.A., Lagoudas, D.C., 2000. Thermomechanical characterization of NiTiCu and NiTi SMA actuators: influence of plastic strains. Smart Mater. Struct. 9, 640.
Miller, R., Phillips, R., 1996. Critical analysis of local constitutive models for slip and decohesion. Philos. Mag. A 73, 803–827.
Mishin, Y., 2004. Atomistic modeling of the γ and γ'-phases of the Ni–Al system. Acta Mater. 52, 1451–1467.
Mitchell, T.E., Foxall, R.A., Hirsch, P.B., 1963. Work-hardening in niobium single crystals. Philos. Mag. 8, 1895–1920.
Miyazaki, S., Imai, T., Igo, Y., Otsuka, K., 1986. Effect of cyclic deformation on the pseudoelasticity characteristics of Ti-Ni alloys. Metall. Trans. A 17, 115–120.
Nabarro, F.R.N., 1947a. Dislocation in a simple cubic lattice. Proc. Phys. Soc. 59.
Nabarro, F.R.N., 1947b. Dislocations in a simple cubic lattice. Proc. Phys. Soc. 59, 256.
Paidar, V., Pope, D.P., Vitek, V., 1984. A theory of the anomalous yield behavior in L12 ordered alloys. Acta Metall. 32, 435–448.
Paier, J., MM, Hummer, K., Kressse, G., Gerber, C., Angyan, J., 2006. Screened hybrid density functionals applied to solids. J. Chem. Phys. 124, 154709.
Paolo, G., Stefano, B., Nicola, B., Matteo, C., Roberto, C., Carlo, C., Davide, C., Guido, L.C., Matteo, C., Ismaila, D., Andrea Dal, C., Stefano de, G., Stefano, F., Guido, F., Ralph, G., Uwe, G., Christos, G., Anton, K., Michele, L., Layla, M.-S., Nicola, M., Francesco, M., Riccardo, M., Stefano, P., Alfredo, P., Lorenzo, P., Carlo, S., Sandro, S., Gabriele, S., Ari, P.S., Alexander, S., Paolo, U., Renata, M.W., 2009. QUANTUM ESPRESSO: a modular and open-source software project for quantum simulations of materials. J. Phys. Condens. Matter 21, 395502.
Patoor, E., El Amrani, M., Eberhardt, A., Berveiller, M., 1995. Determination of the origin for the dissymmetry observed between tensile and compression tests on shape memory alloys. Le J. de Physique IV 5. C2–495-C492-500.

Patra, A., Zhu, T., McDowell, D.L., 2014. Constitutive equations for modeling non-Schmid effects in single crystal bcc-Fe at low and ambient temperatures. Int. J. Plasticity 59, 1–14.
Peach, M., Koehler, J.S., 1950. The forces exerted on dislocations and the stress fields produced by them. Phys. Rev. 80, 436–439.
Peierls, R., 1940. The size of a dislocation. Proc. Phys. Soc. 52, 34.
Plimpton, S., 1995. Fast parallel algorithms for short-range molecular dynamics. J. Comput. Phys. 117, 1–19.
Qin, Q., Bassani, J.L., 1992. Non-schmid yield behavior in single crystals. J. Mech. Phys. Solids 40, 813–833.
Ren, G., Sehitoglu, H., 2016. Interatomic potential for the NiTi alloy and its application. Comput. Mater. Sci. 123, 19–25.
Saleeb, A.F., Padula Ii, S.A., Kumar, A., 2011. A multi-axial, multimechanism based constitutive model for the comprehensive representation of the evolutionary response of SMAs under general thermomechanical loading conditions. Int. J. Plasticity 27, 655–687.
Schmid, Boas, W., 1950. Plasticity of Crystals. A.Hughes and Co., London.
Schulson, E.M., Teghtsoonian, E., 1969. Slip geometry in the body-centred cubic compound β′AuZn. Philos. Mag. 19, 155–168.
Sedmák, P., Šittner, P., Pilch, J., Curfs, C., 2015. Instability of cyclic superelastic deformation of NiTi investigated by synchrotron X-ray diffraction. Acta Mater. 94, 257–270.
Sehitoglu, H., Karaman, I., Anderson, R., Zhang, X., Gall, K., Maier, H.J., Chumlyakov, Y., 2000. Compressive response of NiTi single crystals. Acta Mater. 48, 3311–3326.
Sehitoglu, H., Anderson, R., Karaman, I., Gall, K., Chumlyakov, Y., 2001. Cyclic deformation behavior of single crystal NiTi. Mater. Sci. Eng. A 314, 67–74.
Sehitoglu, H., Hamilton, R., Canadinc, D., Zhang, X., Gall, K., Karaman, I., Chumlyakov, Y., Maier, H., 2003. Detwinning in NiTi alloys. Metallurgical Mater. Trans. A 34, 5–13.
Sehitoglu, H., Wu, Y., Patriarca, L., 2017a. Shape memory functionality under multi-cycles in NiTiHf. Scr. Mater. 129, 11–15.
Sehitoglu, H., Wu Y., Alkan, S., Ertekin, E., 97, 217-228, 2017b. Plastic Deformation of B2-NiTi- Is it Slip or Twinning? Philosophical Magazine Letters.
Sherwood, P.J., Guiu, F., Kim, H.C., Pratt, P.L., 1967. Plastic anisotropy of tantalum, niobium, and molybdenum. Can. J. Phys. 45, 1075–1089.
Simon, T., Kroger, A., Somsen, C., Dlouhy, A., Eggeler, G., 2010. On the multiplication of dislocations during martensitic transformations in NiTi shape memory alloys. Acta Mater. 58, 1850–1860.
Sittner, P., Lukás, P., Neov, D., Novák, V., Toebbens, D., 2003. In situ neutron diffraction studies of martensitic transformations in NiTi, Journal de Physique IV (Proceedings). EDP Sci. 709–711.
Strnadel, B., Ohashi, S., Ohtsuka, H., Miyazaki, S., Ishihara, T., 1995. Effect of mechanical cycling on the pseudoelasticity characteristics of Ti-Ni and Ti-Ni-Cu alloys. Mater. Sci. Eng. A 203, 187–196.
Stroh, A.N., 1958. Dislocations and cracks in anisotropic elasticity. Philos. Mag. 3, 625–646.
Surikova, N.S., Chumlyakov, Y.I., 2000. Mechanisms of plastic deformation of the titanium nickelide single crystals. Phys. Metals Metallogr. 89, 196.
Suzuki, H., 1968. Motion of dislocations in body-centered cubic crystals. In: Rosenfield, A.R., Hahn, G.T., Bement, A.L., Jaffee, R.I. (Eds.), Dislocation Dynamics.
Tadmor, E.B., Miller, R.E., 2011. Modeling materials - continuum. Atomistic Multiscale Technique.
Taillard, K., Blanc, P., Calloch, S., Lexcellent, C., 2006. Phase transformation yield surface of anisotropic shape memory alloys. Mater. Sci. Eng. A 438–440, 436–440.
Taylor, G.I., 1928. The deformation of crystals of $ \beta $-Brass. Proc. R. Soc. Lond. Ser. A 118, 1–24.
Taylor, G.I., 1934. The mechanism of plastic deformation of crystals. Part I. Theor. Proc. R. Soc. Lond. Ser. A, Contain. Pap. a Math. Phys. Character 145, 362–387.
Vanderbilt, D., 1990. Soft self-consistent pseudopotentials in a generalized eigenvalue formalism. Phys. Rev. B 41, 7892–7895.
Vitek, V., 1974. Theory of the core structures of dislocations in body-centred-cubic metals. Cryst. Lattice Defects 5, 1–34.
Vítek, V., Kroupa, F., 1969. Generalized splitting of dislocations. Philos. Mag. 19, 265–284.
Vítek, V., Perrin, R.C., Bowen, D.K., 1970. The core structure of ½(111) screw dislocations in b.c.c. crystals. Philos. Mag. 21, 1049–1073.
Wang, J., Sehitoglu, H., Maier, H.J., 2014. Dislocation slip stress prediction in shape memory alloys. Int. J. Plasticity 54, 247–266.
Weinberger, C.R., Battaile, C.C., Buchheit, T.E., Holm, E.A., 2012. Incorporating atomistic data of lattice friction into BCC crystal plasticity models. Int. J. Plasticity 37, 16–30.
Willis, J.R., 1967. Second-order effects of dislocations in anisotropic crystals. Int. J. Eng. Sci. 5, 171–190.
Yamaguchi, M., Umakoshi, Y., 1983. Dislocations in B.C.C. Metals and ordered alloys and compounds with B.C.C.-Based ordered structures. In: Paidar, V., L.L. (Eds.), The Structure and Properties of Crystal Defects. Elsevier, Liblice Czechoslovakia.
Yamaguchi, M., Pope, D.P., Vitek, V., Umakoshi, Y., 1981. Planar faults and dislocation dissociations in body-centred-cubic-derivative ordered structures. Philos. Mag. A 43, 1265–1275.
Yoo, M.H., Fu, C.L., 1991. Fundamental aspects of deformation and fracture in high-temperature ordered intermetallics. ISIJ Int. 31, 1049–1062.
Zaki, W., Gu, X., Moumni, Z., Zhang, W., 2016. High-cycle fatigue criterion for shape memory alloys based on shakedown theory. In: ASME 2016 Conference on Smart Materials, Adaptive Structures and Intelligent Systems, 1.
Zope, R.R., Mishin, Y., 2003. Interatomic potentials for atomistic simulations of the Ti-Al system. Phys. Rev. B 68, 024102.